

Article

Photothermal Catalytic Reduction of CO₂ by Cobalt Silicate Heterojunction Constructed from Clay Minerals

Shan Qin ¹, Chengrong Ge ², Xiangming Kong ², Meng Fu ¹, Ziheng Zhuang ^{1,2,*} and Xiazhang Li ^{1,*} 

¹ Jiangsu Key Laboratory of Materials Surface Science and Technology, Changzhou Key Laboratory of Biomass Green, Safe and High Value Utilization, Changzhou University, Changzhou 213164, China

² Changzhou Railway Higher Vocational and Technical School, Changzhou 213011, China

* Correspondence: cczuzh@163.com (Z.Z.); xiazhang@cczu.edu.cn (X.L.)

Abstract: The coupled utilization of solar and thermal energy is considered an efficient way to improve the efficiency of CO₂ reduction. Herein, palygorskite (Pal) clay is as a silicon source, while Co²⁺ is introduced to prepare two-dimensional Co₂SiO₄ nanosheets, and the excess of Co²⁺ leads to the growth of Co₃O₄ on the surface of Co₂SiO₄ to obtain an S-scheme Co₂SiO₄/Co₃O₄-x heterojunction, which facilitates the charge transfer and maintains higher redox potentials. Benefiting from black color and a narrow band gap, the cobalt oxide on the surface can increase the light absorption and produce a local photothermal effect. Under proper thermal activation conditions, the photoelectrons captured by the abundant oxygen vacancies can obtain a secondary leap to the semiconductor conduction band (CB), suppressing the recombination of electron-hole pairs, thus favoring the electron transfer on Co₂SiO₄/Co₃O₄-x. The composites not only have abundant oxygen vacancies, but also have a large specific surface area for the adsorption and activation of CO₂. The yields of CH₃OH on Co₂SiO₄/Co₃O₄-5% reach as high as 48.9 μmol·g⁻¹·h⁻¹ under simulated sunlight irradiation. In situ DRIFTS is used to explore the photocatalytic reduction CO₂ mechanism. It is found that the thermal effect facilitates the generation of the key intermediate COOH* species. This work provides a new strategy for photothermal catalytic CO₂ reduction by taking advantage of natural clay and solar energy.

Keywords: photothermal; catalysis; CO₂ reduction; palygorskite; silicate



Citation: Qin, S.; Ge, C.; Kong, X.; Fu, M.; Zhuang, Z.; Li, X. Photothermal Catalytic Reduction of CO₂ by Cobalt Silicate Heterojunction Constructed from Clay Minerals. *Catalysts* **2023**, *13*, 32. <https://doi.org/10.3390/catal13010032>

Academic Editor: Fernando Fresno

Received: 14 November 2022

Revised: 14 December 2022

Accepted: 20 December 2022

Published: 24 December 2022



Copyright: © 2022 by the authors. Licensee MDPI, Basel, Switzerland. This article is an open access article distributed under the terms and conditions of the Creative Commons Attribution (CC BY) license (<https://creativecommons.org/licenses/by/4.0/>).

1. Introduction

With the rapid development of the fossil energy economy, CO₂ emissions are enormous, which disrupts the balance of nature and causes climate change and serious ecological damage in human society [1]. Therefore, research on CO₂ reduction using renewable fuel technology has received widespread attention [2,3].

Inspired by photosynthetic organisms in nature, visible light reduction is used to convert CO₂ into chemicals with high added value and solar fuels (e.g., CO, HCOOH, CH₃OH, CH₄, etc.) [4]. For example, Lin [5] et al. decomposed CO₂ into CO with an apparent quantum yield of 0.25% at 420 nm by using graphitic carbon nitride (g-CN) semiconductors. However, the yield of conventional photocatalytic reduction of CO₂ is generally low, and the difficulties are mainly related to the limited utilization of solar energy and the low efficiency of photogenerated electron/hole separation [6,7]. Recent studies have shown that the introduction of heat in some photocatalytic reactions can effectively enhance reaction performance [8].

Cobalt-based catalysts with full-spectrum absorption performance and multiple valence states are widely used in CO₂ reduction [9]. The modification of Pal clay can significantly change its physical and chemical properties, such as acidification, alkalization, and ion exchange [10]. In our previous work, a unique solar driven catalysis system was developed to convert cellulose into lactic acid using Cu-modified natural palygorskite (Pal)

catalyst [11]. Liu [12] et al. reported on one-dimensional Pal treated with acid to remove most of the metal ions from the silica framework, and bismuth ions were incorporated to grow a two-dimensional (2D) bismuth silicate ($\text{Bi}_{12}\text{SiO}_{20}$) nanosheet under a microwave-hydrothermal process. Metal silicates can be prepared from silica and are often used in cement and glass processing, as well as in manufacturing [13].

Herein, acid modification of 1D Pal was performed to remove most of the metal ions in the Pal skeleton and retain its unique silicon-oxygen tetrahedral structure. A 2D cobalt silicate Co_2SiO_4 was synthesized by the microwave hydrothermal method, in which one-dimensional rod silicate was converted to two-dimensional flake silicate. Cobalt oxide particles were grown on the surface of Co_2SiO_4 by adjusting the amount of Co^{2+} in Co_2SiO_4 . $\text{Co}_2\text{SiO}_4/\text{Co}_3\text{O}_4$ catalysts not only have a large specific surface area, but they also have abundant oxygen vacancies for the adsorption and activation of CO_2 , which effectively achieves full-spectrum absorption and light-induced heat under solar light.

2. Result and Discussion

2.1. XRD

Figure 1a shows the XRD spectra of the Pal, SiO_2 , Co_3O_4 , Co_2SiO_4 , and $\text{Co}_2\text{SiO}_4/\text{Co}_3\text{O}_4$ composites. The peaks located at 8.5° , 20.1° , 28.0° , and 35.8° correspond to the (110), (040), (400), and (161) crystal planes of the original Pal. Compared with the original Pal, the characteristic peaks of acid-treated Pal basically disappeared, indicating that the metal ions in Pal were largely dissolved after a long treatment with high concentrations of hydrochloric acid, corresponding to the SiO_2 . The diffraction peaks appearing at 18.8° , 31.0° , and 36.5° , are ascribed to (111), (220), and (311), crystal planes of Co_2SiO_4 (PDF#29-0508). The characteristic peaks at 31.3° , 36.8° , 44.8° , and 65.2° are consistent with the characteristic peaks of cubic spinel Co_3O_4 (PDF#42-1467). It is noteworthy that the diffraction peaks of Co_3O_4 are very close to Co_2SiO_4 . Figure 1b shows the magnified view of Figure 1a from 36.5° to 39.5° . The peaks of $\text{Co}_2\text{SiO}_4/\text{Co}_3\text{O}_4$ composites are obviously shifted to a higher angle compared with Co_3O_4 and Co_2SiO_4 , indicating a stronger interaction between Co_2SiO_4 and Co_3O_4 [12,14].

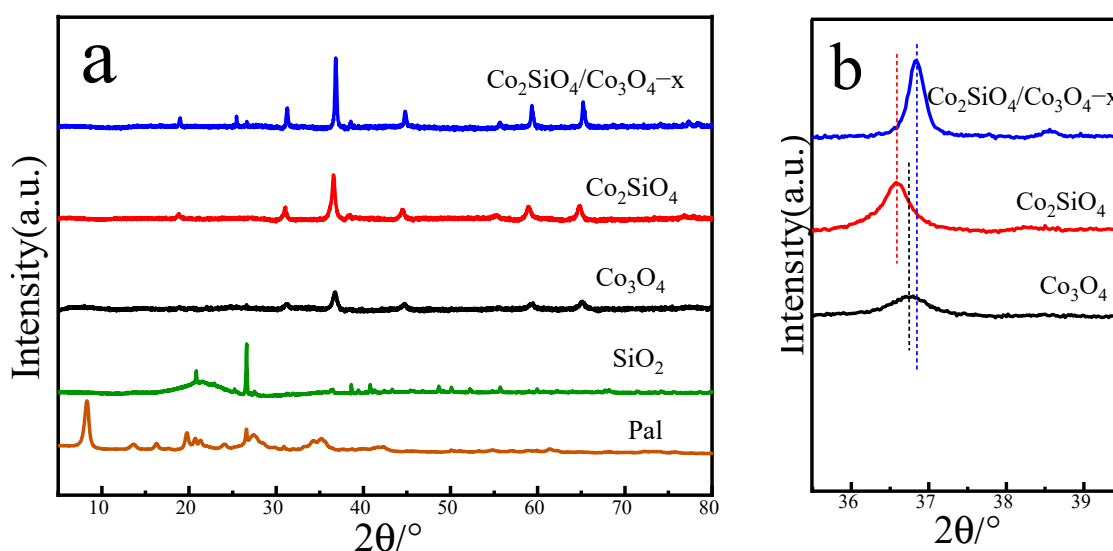


Figure 1. (a) XRD spectra of Pal, SiO_2 , Co_3O_4 , Co_2SiO_4 , and $\text{Co}_2\text{SiO}_4/\text{Co}_3\text{O}_4-x$; (b) enlarged XRD patterns in a 2θ range of 36.5° – 39.5° .

2.2. TEM

Figure 2 shows the TEM picture of the Pal, Co_3O_4 , Co_2SiO_4 , and $\text{Co}_2\text{SiO}_4/\text{Co}_3\text{O}_4$ composites. As shown in Figure 2a, the morphology of Pal is a one-dimensional nanofiber structure with a diameter of about 30–50 nm. After a high concentration of acid treatment, the structure of Pal is destroyed, and the rod-like structure tends to break and assemble into

sheets. Figure 2b,f indicates TEM and HRTEM of Co_2SiO_4 . The microstructure of Co_2SiO_4 is a two-dimensional flake, which may be due to the preservation of the silicon-oxygen tetrahedron structure in the skeleton after the destruction of Pal [12]. After the addition of Co^{2+} , the chain-like structure of the silicon-oxygen tetrahedron regularly grows into two-dimensional cobalt silicate flakes under alkaline hydrothermal conditions. The lattice spacing of the Co_2SiO_4 is 0.09 nm, corresponding to the (400) crystal plane of Co_2SiO_4 . Figure 2c,g displays TEM and HRTEM of $\text{Co}_2\text{SiO}_4/\text{Co}_3\text{O}_4$ –1%, respectively. It can be seen that, on the surface of Co_2SiO_4 , the Co_3O_4 particles have a diameter of about 10 nm. Figure 2d,h shows TEM and HRTEM of $\text{Co}_2\text{SiO}_4/\text{Co}_3\text{O}_4$ –5%; Co_3O_4 particles on the surface of Co_2SiO_4 become more stacked. However, when the amount of Co reaches 10%, it is difficult to distinguish Co_2SiO_4 and Co_3O_4 , as shown in Figure 2e. The HRTEM images (Figure 2g,h) show that the Co_3O_4 nanoparticles are uniformly loaded on the surface of the Co_2SiO_4 2D nanosheets. The lattice spacing of Co_3O_4 on the surface is 0.32 nm and 0.33 nm, corresponding to the (311) and (400) planes of Co_3O_4 , suggesting the existence of a heterogeneous structure between Co_2SiO_4 and Co_3O_4 .

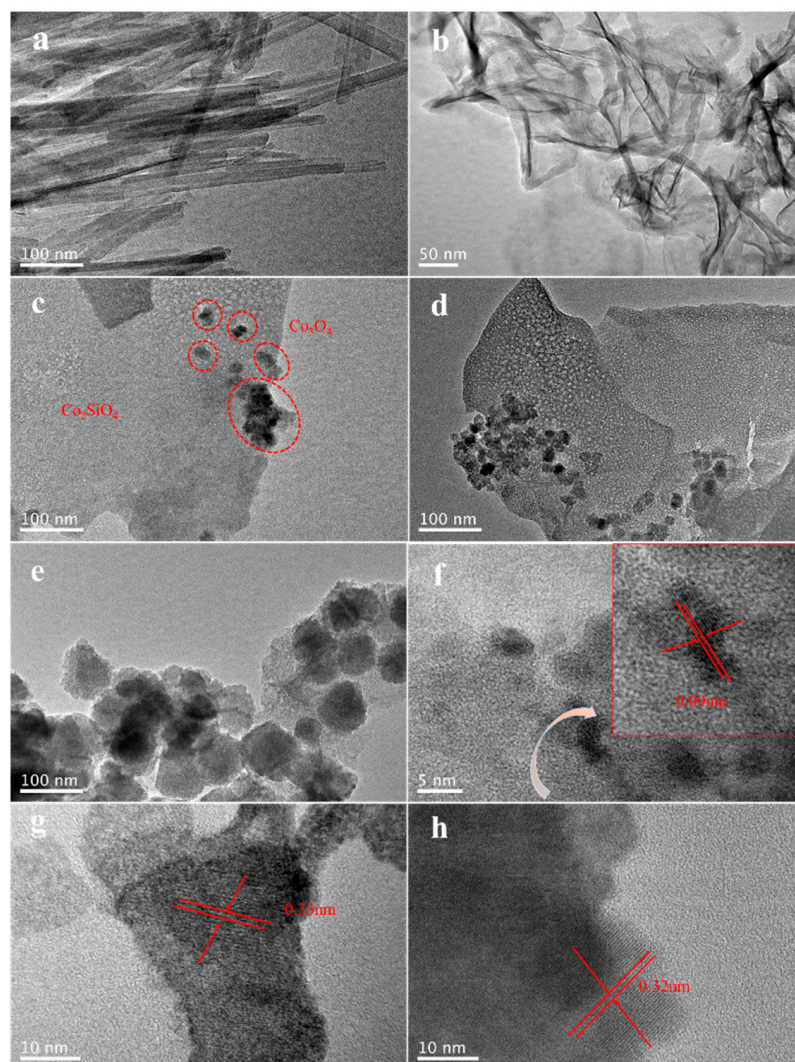


Figure 2. TEM images of (a) Pal, (b) Co_2SiO_4 , (c) $\text{Co}_2\text{SiO}_4/\text{Co}_3\text{O}_4$ –1%, (d) $\text{Co}_2\text{SiO}_4/\text{Co}_3\text{O}_4$ –5%, and (e) $\text{Co}_2\text{SiO}_4/\text{Co}_3\text{O}_4$ –10%. Corresponding HRTEM images of (f) Co_2SiO_4 , (g) $\text{Co}_2\text{SiO}_4/\text{Co}_3\text{O}_4$ –1%, and (h) $\text{Co}_2\text{SiO}_4/\text{Co}_3\text{O}_4$ –5%.

2.3. UV-Vis-NIR

Figure 3a shows the UV-Vis-NIR absorption spectra of the Pal, Co_3O_4 , Co_2SiO_4 , and $\text{Co}_2\text{SiO}_4/\text{Co}_3\text{O}_4$ composites. Pal has a weak UV-Vis-NIR absorption edge of about 380 nm, while Co_2SiO_4 and $\text{Co}_2\text{SiO}_4/\text{Co}_3\text{O}_4$ composites obtained by modifying Pal have full-spectrum absorption to achieve the conversion of UV-responsive natural silicate minerals to visible-responsive silicates. Most of the cobalt-based compounds appear as black or dark green, which can absorb the full range of the spectrum and are ideal photothermal materials [8,15]. The band gaps of Co_2SiO_4 and Co_3O_4 in Figure 3b are estimated by the formula of $(\alpha h\nu)^{n/2} = A(h\nu - E_g)$; where α , h , ν , A , and E_g represent the optical absorption coefficient, Planck constant, optical frequency, a constant, and band gap. The values $n = 1$ and $n = 4$ represent the indirect and direct band gap semiconductors, respectively [16,17]. As shown in Figure 3b, the corresponding band gap energies of Co_2SiO_4 and Co_3O_4 are estimated to be 3.39 and 1.53 eV, respectively. The narrow band gap is more favorable for capturing the energy of sunlight, thus promoting the generation of e^-/h^+ pairs [18].

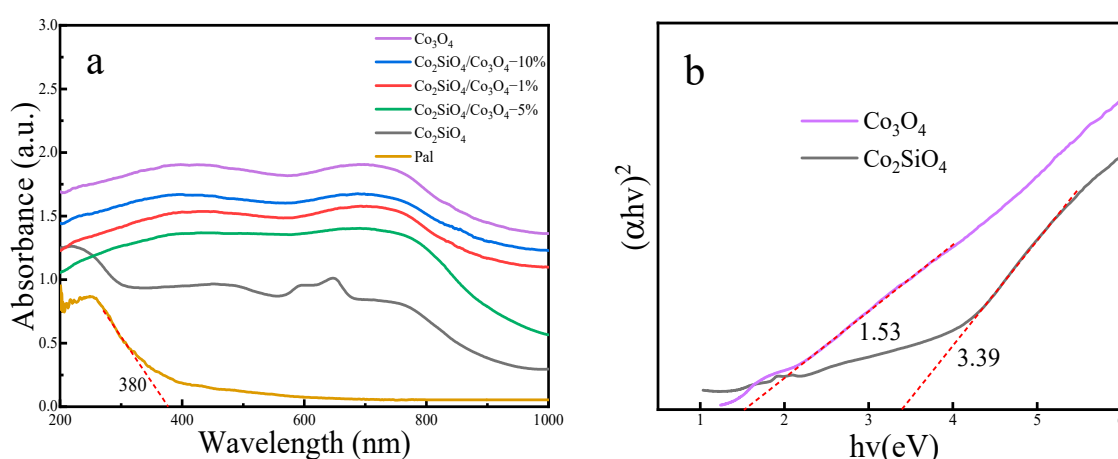


Figure 3. (a) UV-Vis-NIR absorption spectra of Pal, Co_3O_4 , Co_2SiO_4 , and $\text{Co}_2\text{SiO}_4/\text{Co}_3\text{O}_4-x$. (b) Tauc curves of Co_2SiO_4 and Co_3O_4 .

2.4. XPS

Figure 4a shows the XPS survey of Co_3O_4 , Co_2SiO_4 , and $\text{Co}_2\text{SiO}_4/\text{Co}_3\text{O}_4-x$, where the presence of Co and O elements can be determined; Si elements are present in the Co_2SiO_4 and $\text{Co}_2\text{SiO}_4/\text{Co}_3\text{O}_4-x$. Figure 4b shows the Co 2p spectra of Co_3O_4 , Co_2SiO_4 , and $\text{Co}_2\text{SiO}_4/\text{Co}_3\text{O}_4-x$. Co can be divided into four peaks, the peaks with binding energies at 794.59 eV and 795.96 eV correspond to $\text{Co } 2p_{1/2}$. The peaks with binding energies at 779.77 eV and 781.68 eV correspond to $\text{Co } 2p_{3/2}$, suggesting the presence of +2 valence and +3 valence of Co_3O_4 , and also appear in the Co_2SiO_4 and $\text{Co}_2\text{SiO}_4/\text{Co}_3\text{O}_4-x$ [19]. The peaks near the binding energy of 781.06 eV and 797.23 eV in (Figure 4b) correspond to $\text{Co } 2p_{1/2}$ and $\text{Co } 2p_{3/2}$, respectively. Nevertheless, the binding energy of $\text{Co}_2\text{SiO}_4/\text{Co}_3\text{O}_4-x$ is higher than Co_2SiO_4 , which indicates that Co_2SiO_4 has a strong interaction with the additional generated Co_3O_4 , increasing the electron cloud density around Co [20]. The studies show that the binding energy of Co 2p in the Co_2SiO_4 structure is 781.3 eV, while the binding energy of Co 2p in Co_3O_4 is 779.6 eV. Obviously, the binding energy of cobalt is closer to the former, indicating that the product is Co_2SiO_4 , rather than Co_3O_4 , which is consistent with the results of the XRD analysis. In addition, the energy separation between $\text{Co } 2p_{1/2}$ and $\text{Co } 2p_{3/2}$ of the product is 15.96 eV, which is close to Co_2SiO_4 ($\Delta\text{Co } 2p = 15.5$ eV) [21]. Figure 4c shows the O 1s spectra of Co_3O_4 , Co_2SiO_4 , and $\text{Co}_2\text{SiO}_4/\text{Co}_3\text{O}_4-x$. The peaks around the binding energy of 529.85 eV and 532.82 eV correspond to the lattice oxygen (O_L) and adsorbed oxygen (O_A), respectively. The ratio of O_A to O_L in $\text{Co}_2\text{SiO}_4/\text{Co}_3\text{O}_4-x$ is higher than that of Co_3O_4 , indicating the composite $\text{Co}_2\text{SiO}_4/\text{Co}_3\text{O}_4-x$ has higher content of oxygen vacancy than that of Co_3O_4 [22].

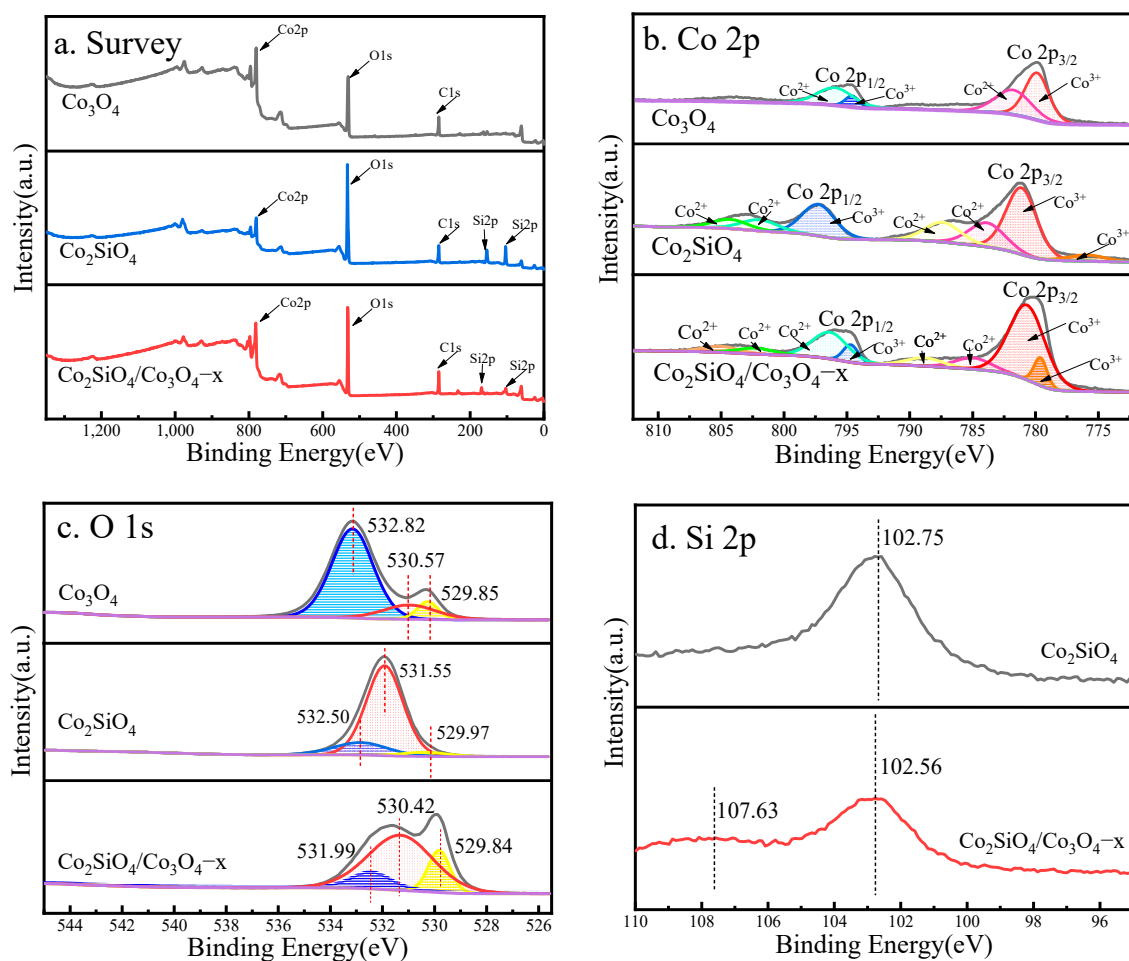


Figure 4. XPS spectra of Co_3O_4 , Co_2SiO_4 , and $\text{Co}_2\text{SiO}_4/\text{Co}_3\text{O}_4-x$: (a) survey spectrum, (b) Co 2p, (c) O 1s, and (d) Si 2p.

Figure 4d shows the Si 2p spectra of Co_2SiO_4 and $\text{Co}_2\text{SiO}_4/\text{Co}_3\text{O}_4-x$. The Si 2p of Co_2SiO_4 is located at the binding energy of 102.75. The Si 2p characteristic peaks of $\text{Co}_2\text{SiO}_4/\text{Co}_3\text{O}_4$ composites exhibit lower binding energy and weaker peaks than Co_2SiO_4 , which may be due to the formation of Si-O-Co bonds on the surface [23].

2.5. EIS, Mott–Schottky Plot, and VB-XPS

Figure 5a indicates that the radius of the electrochemical impedance spectroscopy (EIS) spectrum of the $\text{Co}_2\text{SiO}_4/\text{Co}_3\text{O}_4-5\%$ sample is far less than other counterparts, indicating that the value of resistance is lowest, and the transfer of surface charges is fastest [24,25]. Figure 5b–d exhibits the Mott–Schottky patterns of Co_2SiO_4 , Co_3O_4 , and $\text{Co}_2\text{SiO}_4/\text{Co}_3\text{O}_4-x$. The flat band potentials (E_{fb}) are 0.79, -0.32 , and 0.51 V (vs. Ag/AgCl, pH = 7), respectively, suggesting that their Fermi energy levels are 0.99, -0.12 , and 0.71 V (vs. normal hydrogen electrode (NHE), pH = 7) [26]. Generally, valence band (VB) XPS represents the distance between the valence band and the Fermi level [27]. The VB-XPS of Co_2SiO_4 and Co_3O_4 are shown in Figure 5e,f, which are 1.34 and 0.43 eV. Therefore, the valence bands (E_{VB}) of Co_2SiO_4 and Co_3O_4 are 2.33 and 0.31 V, respectively. According to $E_{CB} = E_{VB} - E_g$, the conduction bands (CBs) of Co_2SiO_4 and Co_3O_4 are calculated to be -1.06 and -1.22 V, respectively.

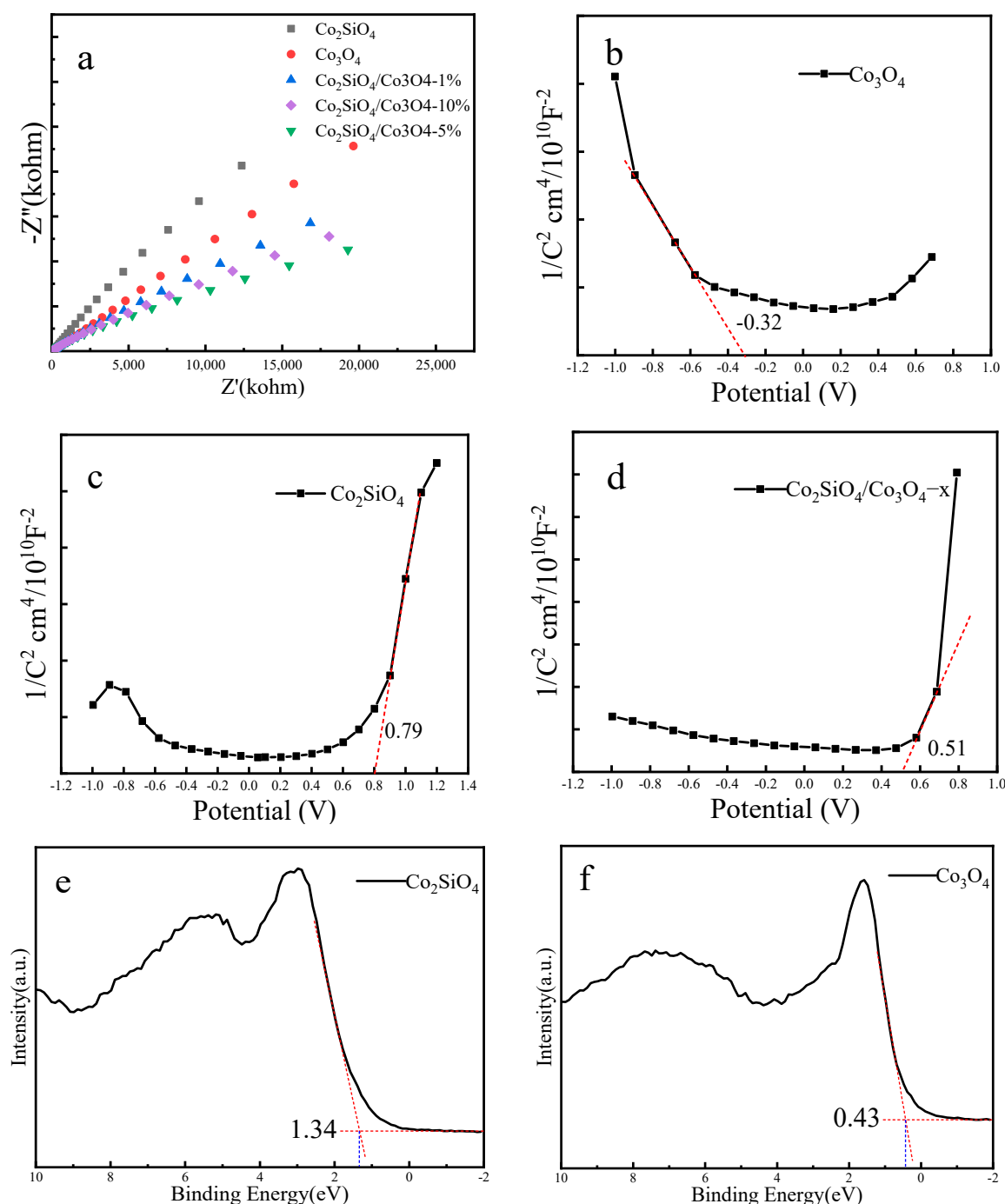


Figure 5. (a) Impedance spectra of Co_3O_4 , Co_2SiO_4 , and $\text{Co}_2\text{SiO}_4/\text{Co}_3\text{O}_4-x$; Mott–Schottky plot of (b) Co_3O_4 , (c) Co_2SiO_4 , and (d) $\text{Co}_2\text{SiO}_4/\text{Co}_3\text{O}_4-x$; VB-XPS of (e) Co_2SiO_4 and (f) Co_3O_4 .

2.6. In-Situ DRIFTS

The reaction pathway of $\text{Co}_2\text{SiO}_4/\text{Co}_3\text{O}_4-x$ was investigated by in situ diffuse reflectance infrared Fourier transform spectroscopy (DRIFTS). The samples are exposed to simulated solar light irradiation (300 W Xe lamp) for 45 minutes, and exporting spectrograms every 5 min. The peak at 2360 cm^{-1} can be attributed to the symmetric stretching vibration modes of CO_2 (Figure 6a) [28]. Figure 6b shows the magnified view of Figure 6a from 1750 cm^{-1} to 1250 cm^{-1} . The peaks from 1600 to 1750 cm^{-1} correspond to the stretching vibration of C–O. The peaks at 1560 and 1540 cm^{-1} can be ascribed to COOH^* species. The peaks at 1455 and 1340 cm^{-1} relate to the O–H bending and C–O stretching vibration

of COOH* groups, respectively [29,30]. It is observed that the peak of COOH* species becomes stronger with increasing light-irradiation time, indicating that the COOH* is one of the key intermediate species for CO₂-to-CH₃OH conversion [31]. Moreover, the signal of CH₂* is detected at 1385 cm⁻¹, confirming the hydrogenation of HCHO* [12]. The IR results show that the photocatalytic reduction of CO₂ on the Co₂SiO₄/Co₃O₄-x surface goes through a sequential process in which COO⁻ and HCHO act as reaction intermediates to generate methanol groups [32]. According to the DRIFTS analysis, a possible CO₂ reduction pathway is summarized in the following reactions [33]:

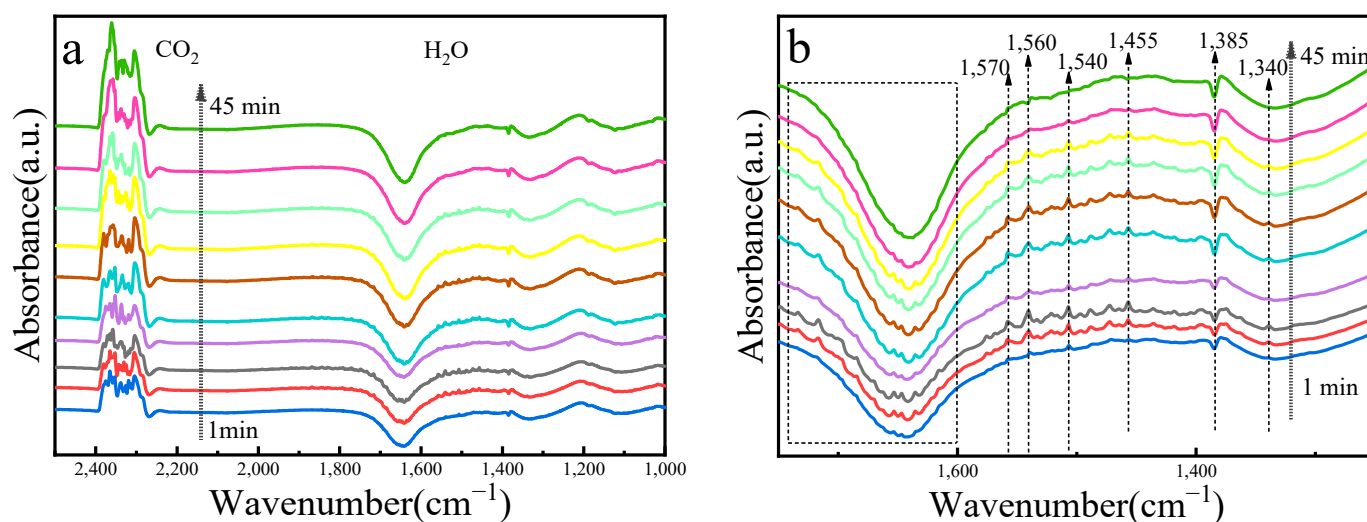
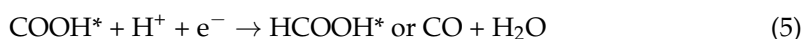
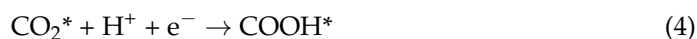
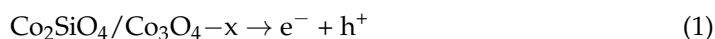


Figure 6. (a) In situ DRIFTS spectra for Co₂SiO₄/Co₃O₄-x; (b) enlarged in situ DRIFTS spectra at a wavenumber range of 1750–1350 cm⁻¹.

2.7. CO₂ Reduction Performance

The photothermal catalytic reduction of CO₂ performance was performed under solar light. The photothermal catalytic CH₃OH generation rate of Co₃O₄, Co₂SiO₄, and Co₂SiO₄/Co₃O₄-x is shown in Figure 7a. For Co₂SiO₄/Co₃O₄-x photocatalysts, the CH₃OH generation rate increases with the increase in Co₃O₄, but excessive Co₃O₄ may inhibit the photocatalytic reduction activity. Co₂SiO₄/Co₃O₄-5% expresses the best CO₂ reduction rates of CH₃OH and CH₄, corresponding to 48.9 and 14.1 μmol·g⁻¹·h⁻¹, which is better than what has been recently reported. After 4 h of sunlight exposure each time, the samples were washed with distilled water for the next test. The samples could maintain considerable photoactivity without significant reduction in activity after five cycling tests (Figure 7b).

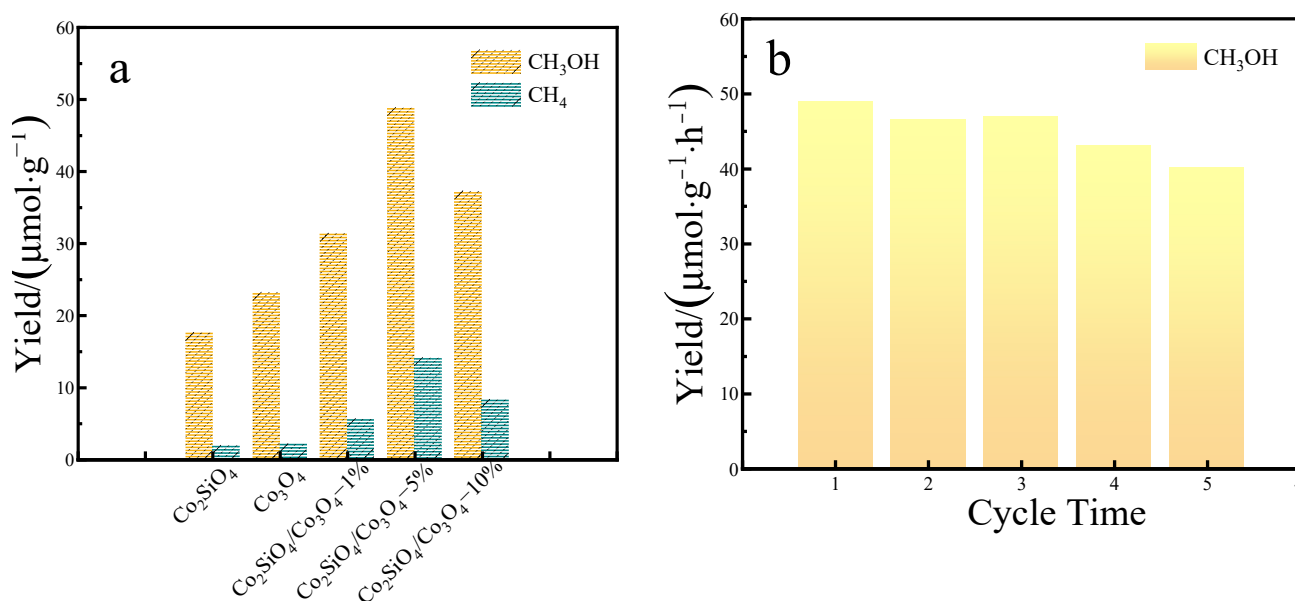


Figure 7. (a) CO₂ reduction performance of Co₃O₄, Co₂SiO₄, and Co₂SiO₄/Co₃O₄-x under solar light; (b) stability of Co₂SiO₄/Co₃O₄-x photothermal CO₂ reduction.

2.8. Schematic Mechanism of Photothermal Catalytic Conversion

Figure 8 demonstrates the photothermal catalytic CO₂ reduction mechanism of Co₂SiO₄/Co₃O₄-x composites. Figure 8a shows the before-contact configuration of the band structures of Co₂SiO₄ and Co₃O₄-x. Co₂SiO₄ has a lower Fermi level than Co₃O₄-x ($E_f = 0.99$), and the free electrons of Co₃O₄-x can be transferred to Co₂SiO₄ until the Fermi reaches equilibrium ($E_f = -0.12$). After contact, the band edge of Co₂SiO₄ with a higher Fermi level bends downward. In comparison, the band edge of Co₃O₄-x with a higher Fermi level bends upward, thus forming a built-in electric field, facilitating the recombination of electrons in Co₂SiO₄ and holes in Co₃O₄-x. The Co₂SiO₄/Co₃O₄-x catalyst has an ultrathin two-dimensional structure with abundant sites for physisorption of CO₂, and abundant oxygen vacancies for chemisorption and activation of CO₂, which facilitates the reduction reaction. Benefiting from a black color and narrow band gap, Co₃O₄-x can increase light absorption and produce a local photothermal effect. Under proper heat activation, the photoelectrons captured by the abundant oxygen vacancies can obtain a secondary leap to the semiconductor conduction band (CB), suppressing the recombination of electron-hole pairs to a certain extent; thus, the energy-rich environment favors the electron transfer on Co₂SiO₄/Co₃O₄-x. Under solar light, Co₂SiO₄/Co₃O₄-x has full-spectrum absorption and can be stimulated to produce e⁻ and h⁺ pairs. The photogenerated e⁻ in the CB of Co₂SiO₄ and the photogenerated h⁺ in the VB of Co₃O₄-x recombines, facilitated by the built-in electric field, thus establishing an S-scheme process. Since E_{CB} of Co₃O₄ is more negative than CO₂/CH₃OH (-0.38 eV), the e⁻ in the CB position of Co₃O₄-x is kept converting CO₂ to methanol. Moreover, Co₂SiO₄ has a more positive VB potential energy than H₂O/H⁺ (1.23 eV). The photogenerated holes in the VB of Co₂SiO₄ oxidize H₂O to O₂ and H⁺ ions (Figure 8b).

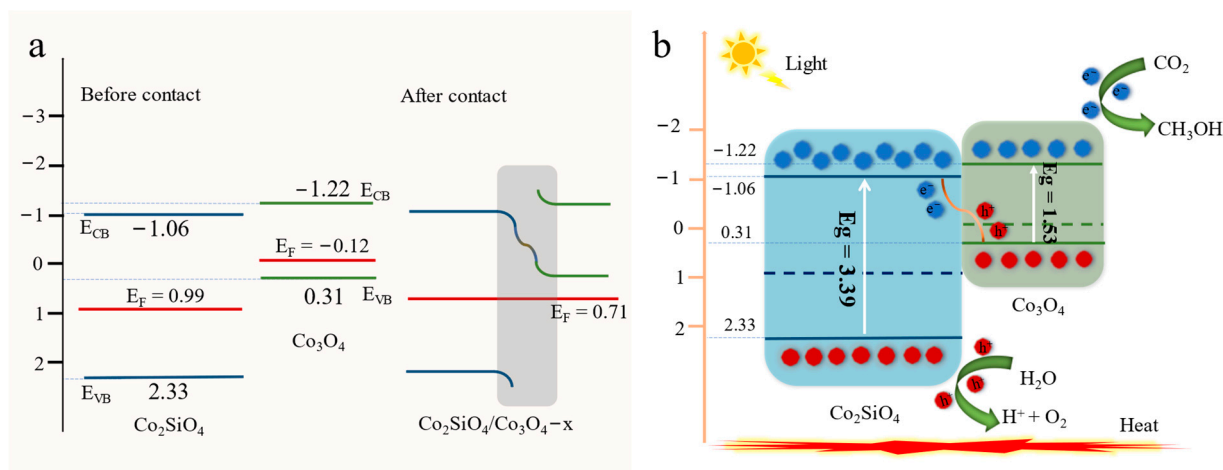


Figure 8. (a) Band structure and transfer route of photogenerated carriers before and after contact between Co_3O_4 and Co_2SiO_4 ; (b) schematic mechanism of photocatalytic conversion of CO_2 over $\text{Co}_2\text{SiO}_4/\text{Co}_3\text{O}_4-x$ heterostructure under sunlight.

3. Experimental Section

3.1. Materials and Chemicals

Raw Pal was obtained from Xuyi, China. Cobalt nitrate ($\text{Co}(\text{NO}_3)_2 \cdot 6\text{H}_2\text{O}$), ammonium sulfate ($(\text{NH}_4)_2\text{SO}_4$), ammonium chloride (NH_4Cl), ammonia ($\text{NH}_3 \cdot \text{H}_2\text{O}$), and hydrochloric acid (HCl) were provided by Shanghai Lingfeng chemical company.

3.2. Preparation of SiO_2

An amount of 10 g of Pal was mixed with 30 g of ammonium sulfate and placed in a ceramic crucible. The mixtures were calcined in a muffle furnace at 500°C for 2 h. An amount of 200 mL 0.5 M HCl was added with refluxing and stirring in a water bath at 80°C for 6 h. After washing and drying, the SiO_2 powders were obtained.

3.3. Preparation of Co_2SiO_4 and $\text{Co}_2\text{SiO}_4/\text{Co}_3\text{O}_4$

An amount of 0.3 g modified Pal was mixed with 10 mmol $\text{Co}(\text{NO}_3)_2 \cdot 6\text{H}_2\text{O}$ in a beaker; 20 mmol NH_4Cl was added after 2 h, and then 1 mL ammonia was added drop by drop to adjust the pH. The solution was transferred into a 100 mL microwave hydrothermal reactor for hydrothermal treatment at 160°C for 90 min. After the reaction, the samples were centrifuged, washed, dried overnight, and the Co_2SiO_4 was obtained.

The preparation method of $\text{Co}_2\text{SiO}_4/\text{Co}_3\text{O}_4-x$ composite material was the same as Co_2SiO_4 , except the quantity of $\text{Co}(\text{NO}_3)_2 \cdot 6\text{H}_2\text{O}$ was adjusted to deposit Co_3O_4 . The different mass ratios in the composite material were denoted as $\text{Co}_2\text{SiO}_4/\text{Co}_3\text{O}_4-x$; where x represents the theoretical mass fraction of Co_3O_4 in the composite from 1% to 10%. The preparation of pure Co_3O_4 was the same as this method without the addition of SiO_2 .

3.4. Catalyst Characterizations

The XRD was used to measure the phase structure of materials on a Rigaku D/max 2500PC (Rigaku Corporation, Tokyo, Japan) diffractometer using $\text{Cu-K}\alpha$ radiation ($\lambda = 1.5406 \text{ \AA}$) with a scanning range of 2θ from 5° to 80° . The TEM was operated on a JEOL-2100 (Japan Electronics Co., Ltd., Tokyo, Japan) with 200 kV working voltage. The UV-vis-NIR was carried out to measure the optical properties of materials with an integrating sphere (UV-3600, DRS, SHIMADZU, Kyoto, Japan). The XPS was performed on a Quantum 2000 Scanning ESCA Microprobe instrument (Thermo Nicolet Evolution, Thermo Fisher, Waltham, MA, USA). The photocurrent response and Mott-Schottky measured the optical properties of materials using an electrochemical workstation equipped with a 300 W Xe lamp and standard three electrodes (Auto Lab 302N, CH Instruments, Shanghai, China). In

situ DRIFTS was conducted by in situ FT-IR spectrometer (Nicolet iS20 FT-IR, ThermoFisher, USA), with a specific designed reaction cell and MCT detector with 120 scans and a resolution of 4 cm^{-1} .

3.5. Photothermal Catalytic CO₂ Reduction Experiments

The photothermocatalytic activity of the samples was carried out in a closed photochemical reactor coupled with a condensation system and gas chromatography. First, 0.1 g of catalysts were added into 100 mL of water in the bottle in the reactor. After sealing, the reactor was infiltrated with CO₂ gas (99.99%) for 45 min to ensure that the reactor was filled with pure CO₂ and to remove the impurity gasses. Then, at room temperature, a xenon lamp was irradiated through the transparent window (diameter 30~40 mm) on the top of the visible reactor. During the reaction process, the temperature in the reactor was monitored, the reaction sampling interval was 30 min, while the mixture product was obtained from the photochemical reactor with a syringe, and the gaseous product was taken out with a gastight needle. The reaction product was detected by a gas chromatograph (GC-7860 Plus, Shanghai Xinuo Instrument Co., Ltd., Shanghai, China) with a flame ionization detector (FID) and a thermal conductivity detector (TCD).

4. Conclusions

In summary, a novel cobalt silicate nanosheet composite (Co₂SiO₄/Co₃O₄-x) was prepared using Pal clay as a silicon source. The acid-modified Pal removed most of the metal ions and retained its unique silicon-oxygen tetrahedral structure, then Co²⁺ were incorporated to acquire Co₂SiO₄ nanosheet and Co₂SiO₄/Co₃O₄-x heterojunction, which realized the conversion of one-dimensional rod silicate to two-dimensional flake silicate. Co₂SiO₄/Co₃O₄-x not only have abundant oxygen vacancies, but also have large specific surface areas for the adsorption and activation of CO₂. The yields of CH₃OH on Co₂SiO₄/Co₃O₄-5% were as high as $48.9\ \mu\text{mol}\cdot\text{g}^{-1}\cdot\text{h}^{-1}$ under simulated sunlight irradiation. In addition, in situ diffuse reflectance infrared Fourier transform spectroscopy (DRIFTS) was used to explore the photocatalytic reduction CO₂ mechanism. Co₂SiO₄/Co₃O₄-x effectively and stably achieved full-spectrum absorption and light-induced heat under solar light. The photothermal synergistic effect facilitated the generation of key intermediate COOH* species to enhance methanol production. This work provides a new approach for photothermal catalytic CO₂ reduction by taking advantage of natural clay and solar energy.

Author Contributions: Methodology, X.K.; Software, M.F.; Validation, Z.Z.; Investigation, S.Q.; Data curation, C.G.; Writing—original draft, S.Q.; Writing—review & editing, X.L.; Project administration, X.L. All authors have read and agreed to the published version of the manuscript.

Funding: This research was funded by the Jiangsu Province Key Laboratory of Materials Surface Science and Technology and Jiangsu High Institutions Key Basic Research Projects of Natural Science (21KJA430002). We thank the Analysis and Testing Center of Changzhou University for the characterization.

Data Availability Statement: Data can be available on request.

Conflicts of Interest: The authors declare no conflict of interest.

References

1. Zuo, S.; Zhang, H.; Li, X.; Han, C.; Yao, C.; Ni, C. Dual Active Sites Boosting Photocatalytic Nitrogen Fixation over Upconversion Mineral Nanocomposites under the Full Spectrum. *ACS Sustain. Chem. Eng.* **2022**, *10*, 1440–1450. [[CrossRef](#)]
2. Zhai, Y.; Han, P.; Yun, Q.; Ge, Y.; Zhang, X.; Chen, Y.; Zhang, H. Phase engineering of metal nanocatalysts for electrochemical CO₂ reduction. *eScience* **2022**, *2*, 467–485. [[CrossRef](#)]
3. Navarro-Jaén, S.; Virginie, M.; Bonin, J.; Robert, M.; Wojcieszak, R.; Khodakov, A.Y. Highlights and challenges in the selective reduction of carbon dioxide to methanol. *Nat. Rev. Chem.* **2021**, *5*, 564–579. [[CrossRef](#)]
4. Zhao, J.; Shi, R.; Waterhouse, G.I.; Zhang, T. Selective photothermal CO₂ reduction to CO, CH₄, alkanes, alkenes over bimetallic alloy catalysts derived from layered double hydroxide nanosheets. *Nano Energy* **2022**, *102*, 107650. [[CrossRef](#)]

5. Lin, J.; Pan, Z.; Wang, X. Photochemical Reduction of CO₂ by Graphitic Carbon Nitride Polymers. *ACS Sustain. Chem. Eng.* **2013**, *2*, 353–358. [[CrossRef](#)]
6. Xu, C.; Anusuyadevi, P.R.; Aymonier, C.; Luque, R.; Marre, S. Nanostructured materials for photocatalysis. *Chem. Soc. Rev.* **2019**, *48*, 3868–3902. [[CrossRef](#)]
7. Liu, Y.; Zhang, C.; Shi, A.; Zuo, S.; Yao, C.; Ni, C.; Li, X. Full solar spectrum driven CO₂ conversion over S-Scheme natural mineral nanocomposite enhanced by LSPR effect. *Powder Technol.* **2021**, *396*, 615–625. [[CrossRef](#)]
8. Gu, Y.; Ding, J.; Tong, X.; Yao, H.; Yang, R.; Zhong, Q. Photothermal catalyzed hydrogenation of carbon dioxide over porous nanosheet Co₃O₄. *J. CO₂ Util.* **2022**, *61*, 102003. [[CrossRef](#)]
9. Zhang, Q.; Yang, P.; Zhang, H.; Zhao, J.; Shi, H.; Huang, Y.; Yang, H. Oxygen vacancies in Co₃O₄ promote CO₂ photoreduction. *Appl. Catal. B Environ.* **2021**, *300*, 120729. [[CrossRef](#)]
10. Sun, L.; Ye, X.; Cao, Z.; Zhang, C.; Yao, C.; Ni, C.; Li, X. Upconversion enhanced photocatalytic conversion of lignin biomass into valuable product over CeVO₄/palygorskite nanocomposite: Effect of Gd³⁺ incorporation. *Appl. Catal. A Gen.* **2022**, *648*, 118923. [[CrossRef](#)]
11. Zhong, M.; Li, X.; Chu, X.; Gui, H.; Zuo, S.; Yao, C.; Li, Z.; Chen, Y. Solar driven catalytic conversion of cellulose biomass into lactic acid over copper reconstructed natural mineral. *Appl. Catal. B Environ.* **2022**, *317*, 121718. [[CrossRef](#)]
12. Liu, Y.; Chu, X.; Shi, A.; Yao, C.; Ni, C.; Li, X. Construction of 2D Bismuth Silicate Heterojunctions from Natural Mineral toward Cost-Effective Photocatalytic Reduction of CO₂. *Ind. Eng. Chem. Res.* **2022**, *61*, 12294–12306. [[CrossRef](#)]
13. Zhu, J.; Xia, L.; Yang, W.; Yu, R.; Zhang, W.; Luo, W.; Dai, Y.; Wei, W.; Zhou, L.; Zhao, Y.; et al. Activating Inert Sites in Cobalt Silicate Hydroxides for Oxygen Evolution through Atomically Doping. *Energy Environ. Mater.* **2021**, *5*, 655–661. [[CrossRef](#)]
14. Long, D.; Li, X.; Yin, Z.; Fan, S.; Wang, P.; Xu, F.; Wei, L.; Tadó, M.O.; Liu, S. Novel Co₃O₄ @ CoFe₂O₄ double-shelled nanoboxes derived from Metal–Organic Framework for CO₂ reduction. *J. Alloys Compd.* **2020**, *854*, 156942. [[CrossRef](#)]
15. Benchikhi, M.; Hattaf, R.; El Ouatif, R. Sol-Gel-Assisted Molten-Salt Synthesis of Co₂SiO₄ Pigments for Ceramic Tiles Application. *Silicon* **2022**, *22*, 1–8. [[CrossRef](#)]
16. Huang, J.; Ye, X.; Li, W.; Shi, A.; Chu, X.; Cao, Z.; Yao, C.; Li, X. Infrared-to-visible upconversion enhanced photothermal catalytic degradation of toluene over Yb³⁺, Er³⁺: CeO₂/attapulgite nanocomposite: Effect of rare earth doping. *J. Ind. Eng. Chem.* **2022**, *116*, 504–514. [[CrossRef](#)]
17. Gao, R.; Shi, A.; Cao, Z.; Chu, X.; Wang, A.; Lu, X.; Yao, C.; Li, X. Construction of 2D up-conversion calcium copper silicate nanosheet for efficient photocatalytic nitrogen fixation under full spectrum. *J. Alloys Compd.* **2022**, *910*, 164869. [[CrossRef](#)]
18. Liu, W.; Li, X.; Chu, X.; Zuo, S.; Gao, B.; Yao, C.; Li, Z.; Chen, Y. Boosting photocatalytic reduction of nitrate to ammonia enabled by perovskite/biochar nanocomposites with oxygen defects and O-containing functional groups. *Chemosphere* **2022**, *294*, 133763. [[CrossRef](#)]
19. Hassen, D.; Shenashen, M.; El-Safty, A.R.; Elmarakbi, A.; El-Safty, S.A. Anisotropic N-Graphene-diffused Co₃O₄ nanocrystals with dense upper-zone top-on-plane exposure facets as effective ORR electrocatalysts. *Sci. Rep.* **2018**, *8*, 3740. [[CrossRef](#)]
20. Bayat, S.; Ghanbari, D.; Salavati-Niasari, M. Pechini synthesis of Co₂SiO₄ magnetic nanoparticles and its application in photo-degradation of azo dyes. *J. Mol. Liq.* **2016**, *220*, 223–231. [[CrossRef](#)]
21. Shepit, M.; Paidi, V.K.; Roberts, C.A.; Lierop, V.J. Competing ferro-and antiferromagnetic exchange drives shape-selective nanomagnetism. *Sci Rep.* **2020**, *10*, 20990. [[CrossRef](#)] [[PubMed](#)]
22. Alhogbi, B.G.; Aslam, M.; Hameed, A.; Qamar, M.T. The efficacy of Co₃O₄ loaded WO₃ sheets for the enhanced photocatalytic removal of 2,4,6-trichlorophenol in natural sunlight exposure. *J. Hazard. Mater.* **2020**, *397*, 122835. [[CrossRef](#)] [[PubMed](#)]
23. Bayat, S.; Sobhani, A.; Salavati-Niasari, M. Co₂SiO₄ nanostructures: New simple synthesis, characterization and investigation of optical property. *Mater. Res. Bull.* **2017**, *88*, 248–257. [[CrossRef](#)]
24. Zheng, Y.L.; Zhou, L.; Sun, X.C.; Zhang, Q.; Yin, H.J.; Du, P.; Yang, X.F.; Zhang, Y.W. Visible-Light Driven CO₂ Reduction to CO by Co₃O₄ Supported on Tungsten Oxide. *J. Phys. Chem. C* **2022**, *126*, 3017–3028. [[CrossRef](#)]
25. Wang, Z.; Zheng, Z.; Xue, Y.; He, F.; Li, Y. Acidic Water Oxidation on Quantum Dots of IrO_x /Graphdiyne. *Adv. Energy Mater.* **2021**, *11*, 2101138. [[CrossRef](#)]
26. Li, X.; Wang, Z.; Chu, X.; Gao, B.; Zuo, S.; Liu, W.; Yao, C. Broad spectrum photo-driven selective catalytic reduction of NO over CeO₂-CeVO₄/palygorskite nanocomposite with enhanced SO₂ tolerance. *Appl. Clay Sci.* **2020**, *199*, 105871. [[CrossRef](#)]
27. He, C.; Li, X.; Qiu, D.; Chen, Y.; Lu, Y.; Cui, X. Nonlinear optical polarization and heterostructure synergistically boosted the built-in electric field of CeF₃/LiNbO₃ for a higher photocatalytic nitrogen reduction activity. *Appl. Surf. Sci.* **2021**, *556*, 149753. [[CrossRef](#)]
28. Wu, Y.; Yan, L.; Yu, Y.; Jing, C. Photocatalytic CO₂ reduction to CH₄ on iron porphyrin supported on atomically thin defective titanium dioxide. *Catal. Sci. Technol.* **2021**, *11*, 6103–6111. [[CrossRef](#)]
29. Liu, W.; Xiang, W.; Guan, N.; Cui, R.; Cheng, H.; Chen, X.; Song, Z.; Zhang, X.; Zhang, Y. Enhanced catalytic performance for toluene purification over Co₃O₄/MnO₂ catalyst through the construction of different Co₃O₄-MnO₂ interface. *Sep. Purif. Technol.* **2021**, *278*, 119590. [[CrossRef](#)]
30. Bian, H.; Liu, T.; Li, D.; Xu, Z.; Lian, J.; Chen, M.; Yan, J.; Liu, S.F. Unveiling the effect of interstitial dopants on CO₂ activation over CsPbBr₃ catalyst for efficient photothermal CO₂ reduction. *Chem. Eng. J.* **2022**, *435*, 135071. [[CrossRef](#)]
31. Cao, G.; Ye, X.; Duan, S.; Cao, Z.; Zhang, C.; Yao, C.; Li, X. Plasmon enhanced Sn:In₂O₃/attapulgite S-scheme heterojunction for efficient photothermal reduction of CO₂. *Colloids Surf. A Physicochem. Eng. Asp.* **2022**, *656*, 130398. [[CrossRef](#)]

32. Bai, S.; Qiu, H.; Song, M.; He, G.; Wang, F.; Liu, Y.; Guo, L. Porous fixed-bed photoreactor for boosting C–C coupling in photocatalytic CO₂ reduction. *eScience* **2022**, *2*, 428–437. [[CrossRef](#)]
33. Lorber, K.; Djinovic, P. Accelerating photo-thermal CO₂ reduction to CO, CH₄ or methanol over metal/oxide semiconductor catalysts. *iScience* **2022**, *25*, 104107. [[CrossRef](#)] [[PubMed](#)]

Disclaimer/Publisher’s Note: The statements, opinions and data contained in all publications are solely those of the individual author(s) and contributor(s) and not of MDPI and/or the editor(s). MDPI and/or the editor(s) disclaim responsibility for any injury to people or property resulting from any ideas, methods, instructions or products referred to in the content.